Supporting Information

Metal-borohydrides as electrolytes for solid-state Li, Na, Mg and Ca batteries: a first-principles study

Ziheng Lu[a] *and Francesco Ciucci*[a,b,*]

Z. Lu, Prof. F. Ciucci
[a] Department of Mechanical and Aerospace Engineering, The Hong Kong University of Science and Technology, Clear Water Bay, Hong Kong, P. R. China.
[b] Department of Chemical and Biomolecular Engineering, The Hong Kong University of Science and Technology, Clear Water Bay, Hong Kong, P. R. China
E-mail: francesco.ciucci@ust.hk (F. Ciucci).

Supplementary materials

Section 1. Calculation details and supplementary analysis

1. Material systems and crystal structures

For the phases that are already present in the MP database, we directly used the ground-state energies of the MP database. [1] We also added other reported phases from the literature as input. Corresponding references are given in **Table S3**. The cation-exchanged and anion-distorted variations were also considered. All structures were further relaxed before obtaining the final energies. **Table S3** details the input structures.

All the B_xH_y species were calculated in their solid states. Although borohydrides with low molar mass, i.e., BH_3 (B_2H_6), B_5H_7 and B_9H_{11} may exist in their gas phase under battery working conditions, [2] [3]computing their energy in solid states does not qualitatively affect the results. This is because the B_xH_y phases have similar formation enthalpies (the difference is in the order of ~10 meV/atom). Calculating B_xH_y phases in solid or gas phases does not vary the shape and the depth of the convex significantly (~10 meV/atom). The electrochemical window is affected by less than 0.1 V.

2. Elastic constants

The 6x6 elastic tensor is denoted C_{ij}. The compliance tensor S_{ij} is calculated by inversing the 6x6 elastic tensor matrix. The poly-crystalline elastic properties under the Voigt and Reuss limit were calculated using

$$B_V = \frac{1}{9}(C_{11} + C_{22} + C_{33}) + 2(C_{12} + C_{23} + C_{31}) \quad (1)$$

$$G_V = \frac{1}{15}(C_{11} + C_{22} + C_{33}) - (C_{12} + C_{23} + C_{31}) + 3(C_{44} + C_{55} + C_{66}) \quad (2)$$

$$B_R = \frac{1}{(S_{11} + S_{22} + S_{33}) + 2(S_{12} + S_{23} + S_{31})} \quad (3)$$

$$G_R = \frac{15}{(S_{11} + S_{22} + C_{33}) - 4(S_{12} + S_{23} + S_{31}) + 3(S_{44} + S_{55} + S_{66})} \quad (4)$$

where B and G represent the bulk and shear modulus while V and R denote the Voigt and Reuss limit/ The Voigt-Reuss-Hill (VRH) average was calculated using

$$B_{VRH} = \frac{1}{2}(B_R + B_V) \text{ and } G_{VRH} = \frac{1}{2}(G_R + G_V) \quad (5)$$

The Pugh ratio was estimated by G_{VRH}/B_{VRH}.

We should note that since the elastic constants of some phases were also calculated by the MP, we found our results to be consistent with those, see **Table S4**.

3. Nudged elastic band calculations of anion rotation

The rotation barrier of anions in metal borohydrides was estimated using climbing image nudged elastic band (CI-NEB) theory. First, supercells were constructed so that at least 8 anions were included in the simulation box. Then the supercell was fully relaxed (including the lattice constants) until the Hellmann-Feynman forces smaller than 0.01 eV/Å were obtained. After that, the initial paths for CI-NEB calculations were constructed. The paths were set so that one of the anion rotates the smallest degrees to coincide with the initial structure. **Figure S1** illustrates the NEB images of the BH_4^- and $B_{12}H_{12}^{2-}$ rotations. Finally, the CI-NEB calculations were conducted with 3 images until a force convergence of 0.01 eV/Å along the band was reached. The calculations were carried out using the VTST code developed by Henkelman et al. [4]

4. Absolute energy levels and band alignments

The absolute energy levels were calculated using the formalism by Toroker et al. [5 6] which was recently applied to $Li_7La_3Zr_2O_{12}$ garnet. [7] In this method, the vacuum energy

level was included by doing slab-type calculations and aligning energy levels of bulk materials to it. Since the band gap center was proved to be irrelevant with the choice of functionals under the Kohn-Sham formalism, [8] this method allows the use of GGA-PBE functional for the slab model which is more computationally expensive with higher level calculations (e.g. meta-GGA/hybrid functional/Green function) for bulk which is less demanding. Detailed theory and derivation could be found in Toroker et al.'s work.[5] [6] Here we give a brief description of our implementation. First, we cleaved a slab model of $LiBH_4$ along the (1 0 0) direction containing 5 layers of anions, as shown in the inset of **Figure S2**. Then we optimized the structure and obtained the corresponding energy levels. The vacuum level (E_{vacuum}) was obtained from the electrostatic potential within the vacuum regions in the slab model as shown in Fig S2. The conduction band minimum ($E_{CBM-slab}$) and valence band maximum ($E_{VBM-slab}$) of the slab were directed obtained from the computation output (Kohn-Sham eigenvalues). The band gap center of the slab was calculated using $E_{BGC-slab} = (E_{CBM-slab} + E_{VBM-slab})/2$. After obtaining the energy levels of the slab model, we relate the bulk energy levels to the vacuum by setting the $E_{BGC-bulk} = E_{BGC-slab}$. Then, we obtained the CBM and VBM of bulk using $E_{VBM-bulk} = E_{BGC-slab} - 0.5 * E_{gap-bulk}$ and $E_{CBM-bulk} = E_{BGC-slab} + 0.5 * E_{gap-bulk}$ where $E_{gap-bulk}$ is the band gap of the bulk material. All slab calculations were done using the GGA-PBE functional while bulk calculations were done using the meta-GGA functional under the MBJ formalism.

5. Mean square displacements and nuclear densities of molecular dynamics simulations

The mean square displacements cations in $CaB_{12}H_{12}$, $MgB_{12}H_{12}$ and $Na_2B_{10}H_{10}$ at 1000 K were calculated using the following equation:

$$\mathrm{MSD} = \langle(\hat{x} - \hat{x}_0)^2\rangle = \frac{1}{N}\sum_{n=1}^{N}(\hat{x}(t) - \hat{x}(0))^2 \qquad (6)$$

where N is the particle number, $\hat{x}$ is the position of the particle and $\langle\cdot\rangle$ denotes the ensemble average. The nuclear density from molecular dynamics simulations was calculated on evenly distributed 30×30×30 grids. On each grid point, the value was obtained by counting the number of neighboring cations within a radius of 1 Å throughout the simulation that was then divided by the simulation time. This method allowed us to get smooth nuclear density iso-surfaces despite the limited sampling compared with binning.

6. Anion rotations in $CaB_{12}H_{12}$

The potential anion disorder was computationally examined using molecular dynamics simulations. We used $CaB_{12}H_{12}$ to exemplify this. We simulated the systems at 1000 K and 1500 K and the trajectories of B are shown in **Figure S3**. The behavior of B at these two temperatures distinct. At 1000 K, although the scattering is large, B atoms still vibrate around their lattice sites. At 1500 K, the trajectories of B atoms are no longer separate clusters. This indicates a rotational distortion of the anions. It is important to note that, the disorder phase transition indicated here is only qualitative. In reality, such high temperature might lead to decomposition of the borohydrides. The overestimation of the decomposition temperature might be due to the over-binding from DFT, the fixed simulation box, and the lack of surfaces in the model.

7. Pearson correlation coefficient

Pearson correlation coefficient is a measure of the linear correlation between two variables X and Y. It has a value between +1 and –1, where 1 is total positive linear correlation, 0 is no linear correlation, and –1 is total negative linear correlation. [9] In

this work, the Pearson correlation coefficient between anion rotation barriers and phase transition temperatures is calculated using the following equation

$$r = \frac{\sum_{i=1}^{n}(T_i - \overline{T})(\Delta E_i - \overline{\Delta E})}{\sqrt{\sum_{i=1}^{n}(T_i - \overline{T})^2}\sqrt{\sum_{i=1}^{n}(\Delta E_i - \overline{\Delta E})^2}} \quad (7)$$

where r is the Pearson correlation coefficient, T_i is the phase transition temperature of phase i, $\overline{T}$ is the average phase transition temperature of all phases, ΔE_i is the anion rotation barrier of phase i, $\overline{\Delta E}$ is the average anion rotation barrier of all phases.

8. Van Hove correlation analysis of molecular dynamics simulation trajectories

We calculated van Hove correlation function [10] using pymatgen code [11 12] based on the MD trajectories of cations in Na, Mg and Ca borohydrides. Van Hove correlation function can be separated into 2 parts, i.e., the self-part G_s and the distinct-part G_d: [12]

$$G_s(r,t) = \frac{1}{4\pi r^2 N_d}\langle\sum_{i=1}^{N_d}\delta(r - |\mathbf{r}_i(t_0) - \mathbf{r}_i(t+t_0)|)\rangle_{t_0}$$

$$G_d(r,t) = \frac{1}{4\pi r^2 \rho N_d}\langle\sum_{i\neq j}^{N_d}\delta(\vec{r} - |\vec{r}_i(t_0) - \vec{r}_j(t+t_0)|)\rangle_{t_0}$$

where $\delta(\cdot)$ is the Dirac delta function, $\langle\cdot\rangle$ is an average over initial configuration at t_0, $\vec{r}_i(t)$ is the position of ith particle at time t, N_d is the total number of Li, Na, Mg, or Ca in the simulation cell and r is the radial distance. ρ is the average number density which is used to normalize G_d so that it tends to 1 when $r \gg 1$. G_s describes the radial distribution function (rdf) of a particle given its initial position, whereas G_d describes the rdf of all other particles after time t with respect to the initial referenced position.

FigureS8 shows the van Hove correlation function of Na, Mg, and Ca in corresponding borohydrides. For Ca and Mg, the van Hove correlation functions have similar

characteristics. G_s displays high density regions around r = 0.8 Å for all t > 0.4 ps. Since 0.8 Å is significantly smaller than the distance between the nearest cation sites (~7 Å), these high intensity regions could be attributed to the large thermal vibrations. In the distinct part, $G_d(r,t)$ could be reduced to the pair distribution function of cations. The high intensity regions peak around 7 Å, a distance corresponding to the distance between adjacent cation sites. Such characteristics of van Hove correlations reveal that Mg and Ca do not diffuse during simulation.

For Na, from the self-part van Hove correlation, the high-density region spreads after several picoseconds. This indicates that Na ions tend to hop out of their original sites after only a short time. After leaving their original site, the Na ions tend to mix quickly since only shallow peaks around r = 6 Å and r = 8 Å could be found. This is distinctly different from the van Hove self-correlations of fast ionic conductors such as Li_6PS_5Cl where strong peaks could be found after the initial jump[13, 14]. From the distinct-part, a strong peak at r=0.8 Å emerges after about 5 picoseconds. Such characteristics is usually attributed to the strongly correlated motion of Na atoms. [13, 15]

Section 2. Supplementary figures

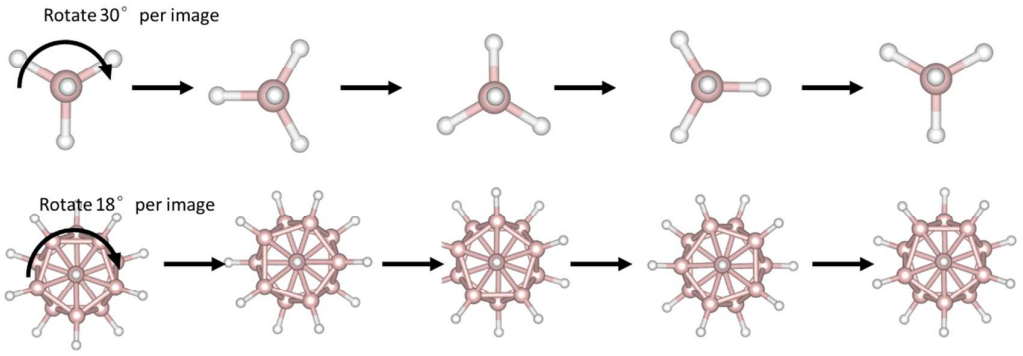

Figure S1. The initial path of the anion rotation for BH_4^- and $B_{12}H_{12}^{2-}$. For BH_4^-, rotation along the C_3 axis leads to the minimum rotated degrees (360°/3=120°) to coincide with the initial structure. Since there are 3 intermediate images, the anion was rotated 30° (120°/4) between each two images. For $B_{12}H_{12}^{2-}$, this angle was 18°(360°/5/4).

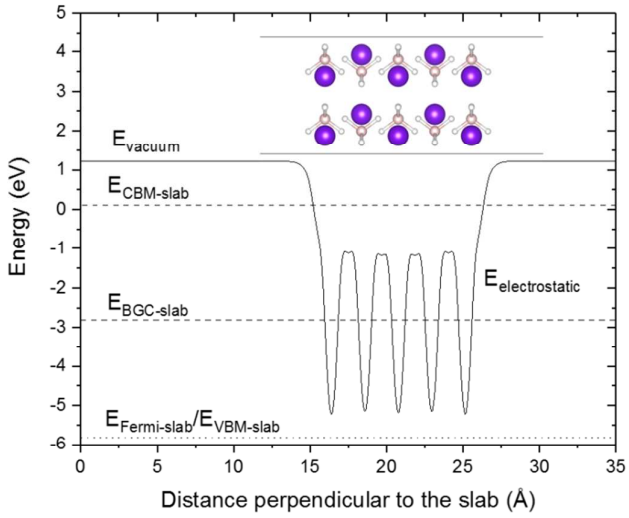

Figure S2. The electrostatic potential and the energy levels pf the slab model for $LiBH_4$. Due to the use of pseudo-potentials in the calculations, only the relative values are meaningful. The inset shows the slab model where white, purple and pink balls represent H, Li and B atoms.

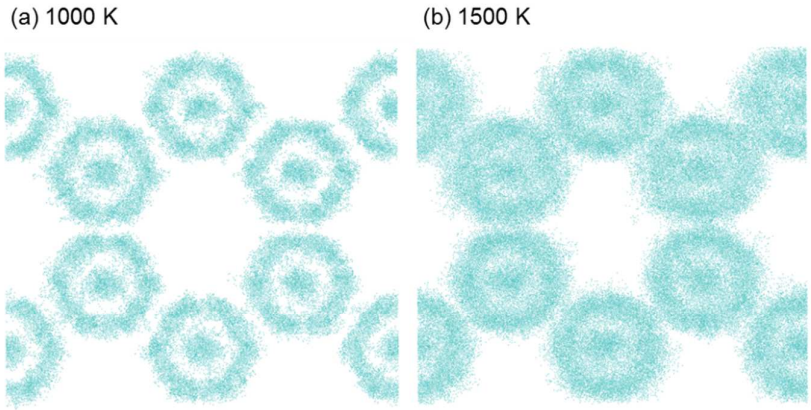

Figure S3. The trajectories of B from a 10 ps molecular dynamics simulation of $CaB_{12}H_{12}$ at (a) 1000 K and (b) 1500 K. The snapshots of B were taken every 10 fs.

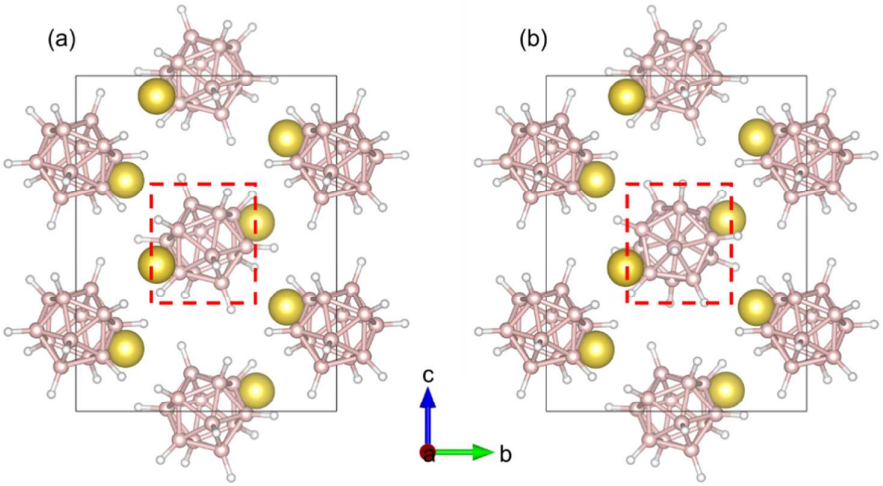

Figure S4. The structure of the (a) ground-state $Na_2B_{12}H_{12}$ and the (b) anion rotated $Na_2B_{12}H_{12}$. The rotated anion is highlighted using the red dashed box. Yellow, pink and white balls represent Na, B and H atoms respectively. Apart from the rotated anion, other atoms were also displaced a little from the original place after the relaxation.

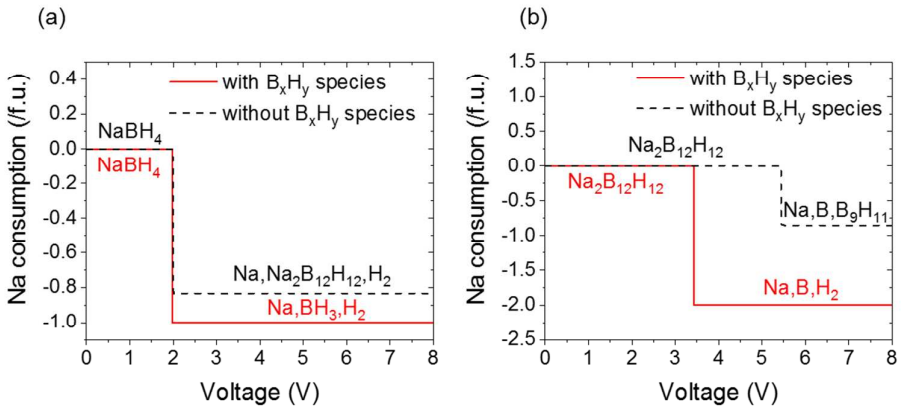

Figure S5. The decomposition product of (a) $NaBH_4$ and (b) $Na_2B_{12}H_{12}$ at different voltages.

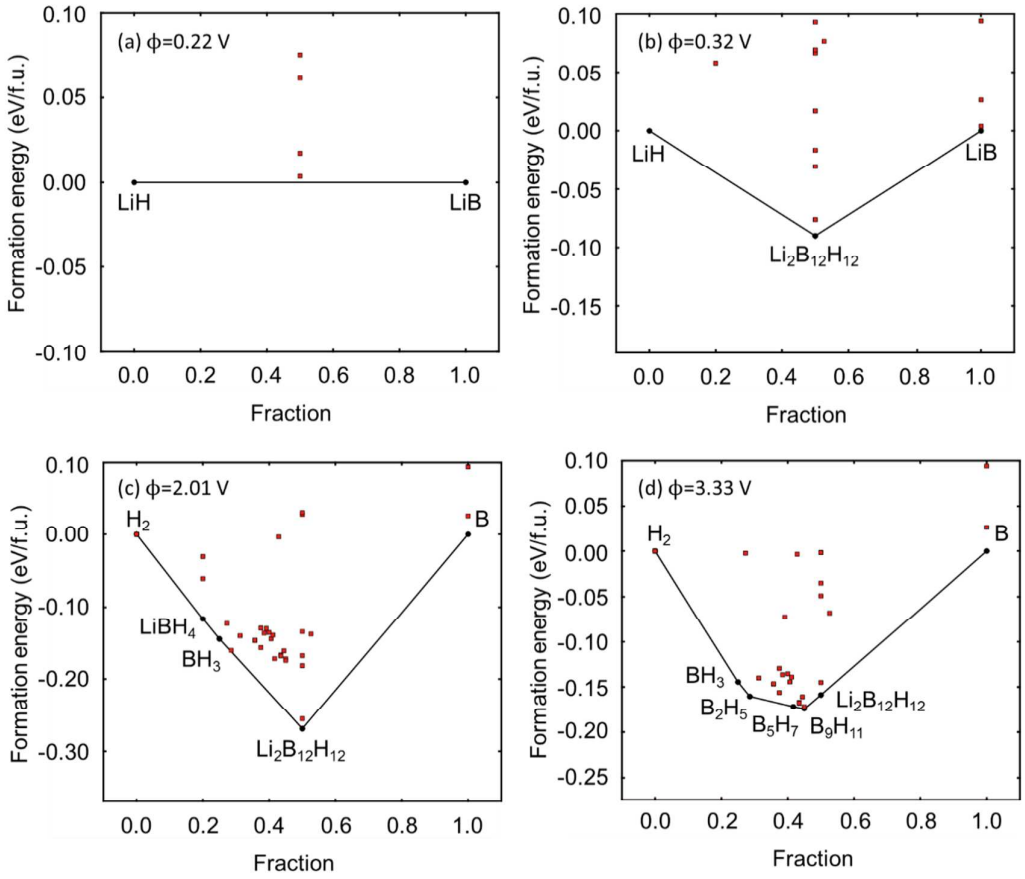

Figure S6. Grand potential phase diagram of the Li-B-H systems at (a) ϕ=0.22 V, (b) ϕ=0.32 V, (c) ϕ =2.01 V, and (d) ϕ =3.33 V. The voltages shown are selected voltages where critical phases ($LiBH_4$ and $Li_2B_{12}H_{12}$) become stable or unstable. For the Na-B-H systems, the diagrams are shown in **Figure S**6.

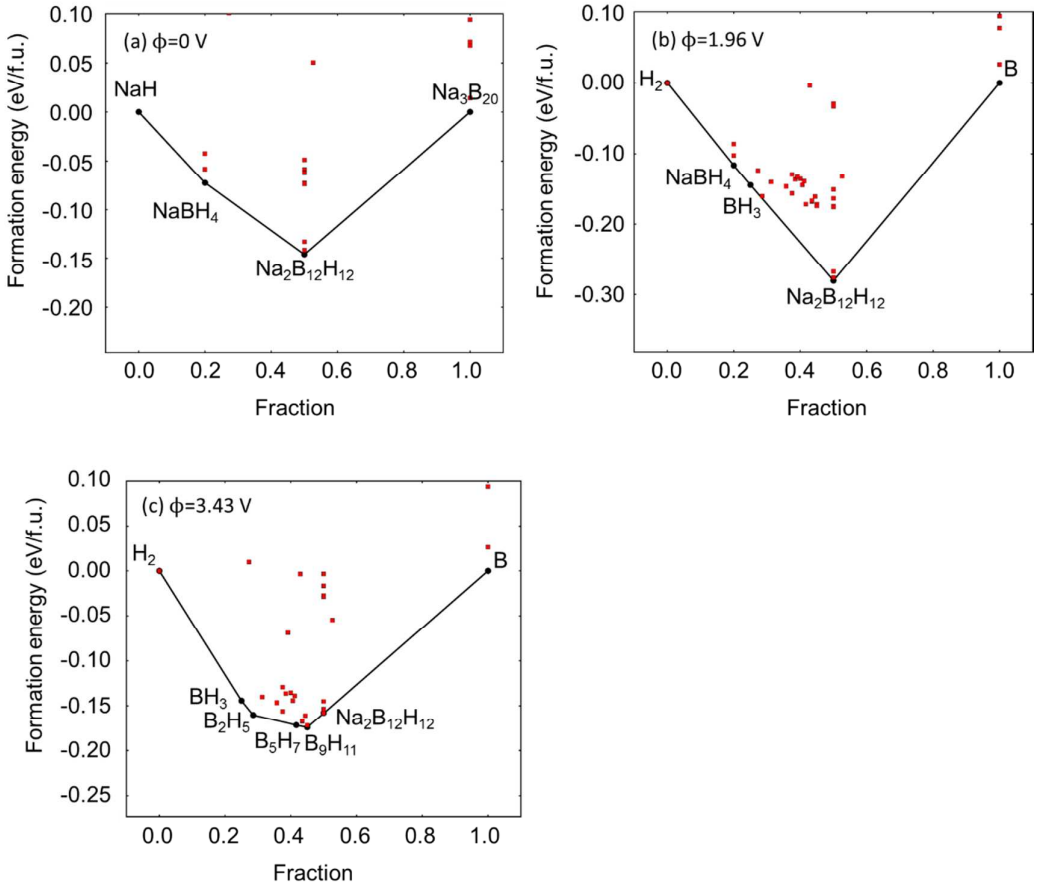

Figure S7. Grand potential phase diagram of Na-B-H systems at (a) ϕ=0 V, (b) ϕ=1.96 V, and (c) ϕ=3.43 V. The choice of voltages shown in these figures was determined where critical phases ($NaBH_4$ and $Na_2B_{12}H_{12}$) start to become stable or unstable.

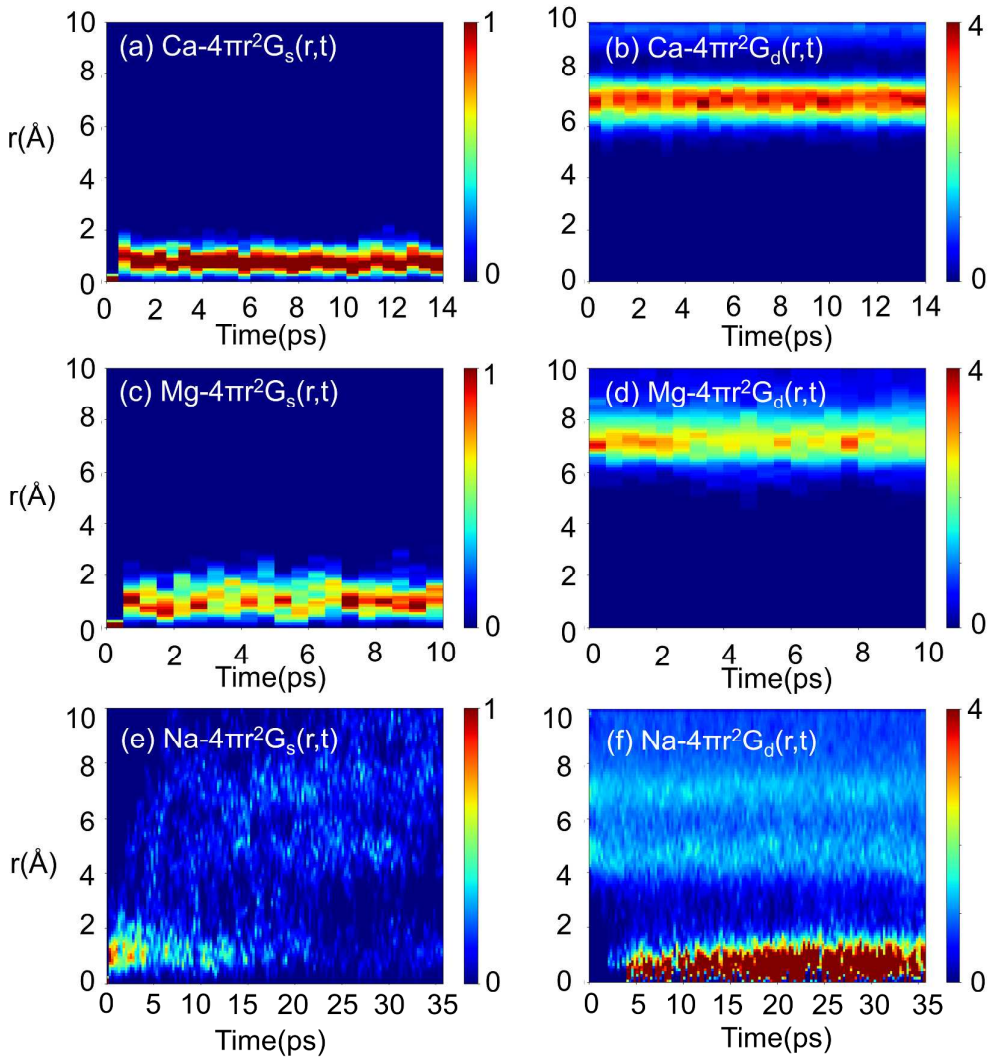

Figure S8. Transformed van Hove correlation of cations in borohydrides. (a), (c), and (e) shows the self-part van Hove correlation of cations in $CaB_{12}H_{12}$, $MgB_{12}H_{12}$ and $Na_2B_{10}H_{10}$, respectively, whereas (b), (d), and (f) shows the distinct-parts.

Section 3. Supplementary tables

Table S1. Lattice parameters (Å) and cell volume (Å^3) for orthorhombic $LiBH_4$

Functional	a	b	c	volume
LDA	6.76	4.18	6.49	183.69
GGA-PBE	7.00	4.37	6.78	207.67
GGA-PBEsol	6.92	4.28	6.65	197.13
GGA-PPE+D3	6.86	4.27	6.60	193.50
Experimental	7.18	4.44	6.80	216.7

Table S2. Energy above hull of stable and meta-stable phases of Li and Na borohydrides

Cation	Composition	Energy above hull (mev/atom)	Cation	Composition	Energy above hull (ev/atom)
Li	$LiBH_4$	0	Na	$NaBH_4$	0
	$Li_2B_{12}H_{12}$	0		$Na_2B_{12}H_{12}$	0
	$Li_2B_{10}H_{10}$	53		$Na_2B_{10}H_{10}$	66
	LiB_3H_8	29		NaB_3H_8	30
	$LiB_{10}H_9$	78		$Na_2B_6H_6$	72

Table S3 The additional structures calculated besides those existing in the MP database.

System	Composition	Reference	Notes
Li-B-H (71 phases)	LiB_3H_8	Ohba et al., 2006 [16]	DFT predicted structure
	LiB_9H_{14}	mp-27590 *	Obtained by substituting all Cs atoms to Li atoms in CsB_9H_{14} (mp-978278)
	$LiB_{10}H_9$	mp-27650	Obtained by substituting all Rb atoms to Li atoms in $RbB_{10}H_9$ (mp-27650)
	$Li_2B_6H_6$	mp-23950	Obtained by substituting all K atoms to Li atoms in $K_2B_6H_6$ (mp-23950)
	$Li_2B_6H_6$	Ohba et al., 2006 [16]	DFT predicted structure
	$Li_2B_{10}H_{10}$	Wu et al., 2015 [17]	Obtained by rotating one of the $B_{10}H_{10}^{2-}$ in $Li_2B_{10}H_{10}$ (Wu et al., 2015 [17])
	$Li_2B_{10}H_{10}$	mp-776332	Obtained by substituting all Na atoms to Li atoms in $Na_2B_{10}H_{10}$ (mp-776332)
	$Li_2B_{10}H_{10}$	Wu et al., 2015 [17]	Structure from neutron powder diffraction and DFT calculations.
	$Li_2B_{12}H_{12}$	Her et al. 2008 [18]	α-$Li_2B_{12}H_{12}$ from powder X-ray diffraction and neutron powder diffraction
	$Li_2B_{12}H_{12}$	mp-978278	Obtained by substituting all Na atoms to Li atoms in $Na_2B_{12}H_{12}$ (mp-978278)
	$Li_2B_{12}H_{12}$	Her et al. 2008 [18]	Obtained by rotating one of the $B_{12}H_{12}^{2-}$ in $Li_2B_{12}H_{12}$ (Her et al. 2008 [18])
	$Li_7B_{48}H_{48}$	Her et al. 2008 [18]	Obtained by removing one Li atom from the supercell of $Li_2B_{12}H_{12}$ (Her et al. 2008 [18])
	$Li_7B_{40}H_{40}$	Wu et al.,	Obtained by removing one Li atom from the

		2015 [17]	supercell of $Li_2B_{10}H_{10}$ (Wu et al., 2015 [17])
	$Li_7B_8H_{32}$	mp-30209	Obtained by removing one Li atom from the supercell of $LiBH_4$ (mp-30209)
Na-B-H (66 phases)	NaB_3H_8	Ohba et al., 2006 [16]	Obtained by substituting all Li atoms to Na from LiB_3H_8 (Ohba et al. [16])
	NaB_9H_{14}	mp-27590	Obtained by substituting all Cs atoms to Na atoms in CsB_9H_{14} (mp-978278)
	$NaB_{10}H_9$	mp-27650	Obtained by substituting all Rb atoms to Na atoms in $RbB_{10}H_9$ (mp-27650)
	$Na_2B_6H_6$	mp-23950	Obtained by substituting all K atoms to Na atoms in $K_2B_6H_6$ (mp-23950)
	$Na_2B_{10}H_{10}$	mp-776332	Obtained by rotating one of the $B_{10}H_{10}^{2-}$ in $Na_2B_{10}H_{10}$ (mp-776332)
	$Na_2B_{10}H_{10}$	Wu et al., 2015 [17]	Obtained by substituting all Li atoms to Na in $Li_2B_{10}H_{10}$ (Wu et al., 2015 [17])
	$Na_2B_{12}H_{12}$	Her et al. 2008 [18]	Obtained by substituting all Li atoms to Na atoms in α-$Li_2B_{12}H_{12}$ (Her et al. 2008 [18])
	$Na_2B_{12}H_{12}$	mp-978278	Obtained by rotating one of the $B_{12}H_{12}^{2-}$ in $Na_2B_{12}H_{12}$ (mp-978278)
	$Na_7B_{48}H_{48}$	mp-978278	Obtained by removing one Li atom from the supercell of $Na_2B_{12}H_{12}$ (mp-978278)
	$Na_7B_{40}H_{40}$	mp-776332	Obtained by removing one Li atom from the supercell of $Na_2B_{10}H_{10}$ (mp-776332)
	$Na_7B_8H_{32}$	mp-38725	Obtained by removing one Li atom from the supercell of $NaBH_4$ (mp-38725)
Mg-B-H (56 phases)	$MgB_{12}H_{12}$	Ozolins et al., 2008 [19]	Crystalline $MgB_{12}H_{12}$ phase using theoretically predicted PEGS algorithm.
	$MgB_{12}H_{12}$	Ozolins et al., 2008 [19]	Obtained by rotating one of the $B_{12}H_{12}^{2-}$ in $MgB_{12}H_{12}$ (Ozolins et al., 2008 [19])
	$MgB_{12}H_{12}$	Ozolins et al., 2008 [19]	Obtained by substitute all Ca atoms to Mg in predicted crystalline $CaB_{12}H_{12}$.
	$MgB_{10}H_{10}$	mp-776332	Obtained by removing half of the Na atoms from $Na_2B_{10}H_{10}$ (mp-776332) and substitute the rest to Mg.
	$Mg_7B_{96}H_{96}$	Ozolins et al., 2008 [19]	Obtained by removing one Ca atom from the supercell of $MgB_{12}H_{12}$
	$Mg_7B_{16}H_{64}$	mp-571156	Obtained by removing one Mg atom from the supercell of $Mg(BH_4)_2$ (mp-776332)
Ca-B-H (58 phases)	$CaB_{12}H_{12}$	Ozolins et al., 2008 [19]	Crystalline $CaB_{12}H_{12}$ phase using theoretically predicted PEGS algorithm. (Ozolins et al., 2008 [19])

	$CaB_{12}H_{12}$	Ozolins et al., 2008 [19]	Obtained by rotating one of the $B_{12}H_{12}^{2-}$ in $CaB_{12}H_{12}$ (Ozolins et al., 2008 [19])
	$CaB_{12}H_{12}$	Ozolins et al., 2008 [19]	Obtained by substitute all Mg atoms to Ca in predicted crystalline $MgB_{12}H_{12}$. (Ozolins et al., 2008 [19])
	$CaB_{10}H_{10}$	mp-776332	Obtained by removing half of the Na atoms from $Na_2B_{10}H_{10}$ (mp-776332) and substitute the rest to Ca.
	$Ca_7B_{96}H_{96}$	Ozolins et al., 2008 [19]	Obtained by removing one Ca atom from the supercell of $CaB_{12}H_{12}$ (Ozolins et al., 2008 [19])
	$Ca_7B_{16}H_{64}$	mp-966591	Obtained by removing one Ca atom from the supercell of $Ca(BH_4)_2$ (mp-966591)

'mp-*****' refers to the object ID in the Materials Project database.

Table S4. Elastic modulus in GPa

Materials	VRH shear modulus this work	VRH shear modulus from MP	VRH Bulk Modulus this work	VRH Bulk Modulus from MP	Reference
Li	4.02	4.60	14.02	13.67	mp-135*
$LiBH_4$	5.12	6.03	14.78	16.03	mp-30209
$Li_2B_{10}H_{10}$	9.39	-	17.27	-	-
$Li_2B_{12}H_{12}$	9.15	-	17.10	-	-
Na	3.62	3.59	8.90	8.87	mp-10172
$NaBH_4$	9.24	10.27	16.27	19.27	mp-38725
$Na_2B_6H_6$	10.77	-	19.80	-	-
$Na_2B_{10}H_{10}$	3.93	-	10.26	-	mp-776332
$Na_2B_{12}H_{12}$	5.31	-	10.52	-	mp-978278

'mp-*****' refers to the object ID in the Materials Project database.

Table S5. Formation energies of cation vacancies

System	Material	Vacancy formation energy from phase equilibria/ cation extraction (eV)	System	Material	Vacancy formation energy from phase equilibria/ cation extraction (eV)
Li-B-H	$LiBH_4$	0.33/0.59	Na-B-H	$NaBH_4$	0.32/0.56
	$Li_2B_{12}H_{12}$	0.14/0.56		$Na_2B_{12}H_{12}$	0.16/0.57
	$Li_2B_{10}H_{10}$	0.62/0.65		$Na_2B_{10}H_{10}$	0.56/0.57

Ca-B-H	$Ca(BH_4)_2$	0.73/1.21	Mg-B-H	$Mg(BH_4)_2$	0.74/1.02
	$CaB_{12}H_{12}$	0.30/1.11		$MgB_{12}H_{12}$	0.62/1.18

References

(1) Jain, A.; Ong, S. P.; Hautier, G.; Chen, W.; Richards, W. D.; Dacek, S.; Cholia, S.; Gunter, D.; Skinner, D.; Ceder, G., Commentary: The Materials Project: A Materials Genome Approach to Accelerating Materials Innovation. *APL Mater.* **2013,** 1, 011002.

(2) Au, M.; Walters, R. T., Reversibility Aspect of Lithium Borohydrides. *Int. J. Hydrogen Energy* **2010,** 35, 10311-10316.

(3) Mohtadi, R.; Orimo, S.-i., The Renaissance of Hydrides as Energy Materials. *Nat. Rev. Mater.* **2016,** 2, 16091.

(4) Henkelman, G.; Uberuaga, B. P.; Jónsson, H., A Climbing Image Nudged Elastic Band Method for Finding Saddle Points and Minimum Energy Paths. *J. Chem. Phys.* **2000,** 113, 9901-9904.

(5) Toroker, M. C.; Kanan, D. K.; Alidoust, N.; Isseroff, L. Y.; Liao, P.; Carter, E. A., First Principles Scheme to Evaluate Band Edge Positions in Potential Transition Metal Oxide Photocatalysts and Photoelectrodes. *Phys. Chem. Phys. Chem.* **2011,** 13, 16644-16654.

(6) Fidelsky, V.; Caspary Toroker, M., Engineering Band Edge Positions of Nickel Oxyhydroxide through Facet Selection. *J. Phys. Chem. C* **2016,** 120, 8104-8108.

(7) Thompson, T.; Yu, S.; Williams, L.; Schmidt, R. D.; Garcia-Mendez, R.; Wolfenstine, J.; Allen, J. L.; Kioupakis, E.; Siegel, D. J.; Sakamoto, J., Electrochemical Window of the Li-Ion Solid Electrolyte $Li_7La_3Zr_2O_{12}$. *ACS Energy Lett.* **2017,** 2, 462-468.

(8) Perdew, J. P.; Levy, M., Physical Content of the Exact Kohn-Sham Orbital Energies: Band Gaps and Derivative Discontinuities. *Phys. Rev. Lett.* **1983,** 51, 1884.

(9) Pearson, K., Note on Regression and Inheritance in the Case of Two Parents. *Proc. R. Soc. London* **1895,** 58, 240-242.

(10) Van Hove, L., Correlations in Space and Time and Born Approximation Scattering in Systems of Interacting Particles. *Phys. Rev.* **1954,** 95, 249.

(11) Ong, S. P.; Richards, W. D.; Jain, A.; Hautier, G.; Kocher, M.; Cholia, S.; Gunter, D.; Chevrier, V. L.; Persson, K. A.; Ceder, G., Python Materials Genomics (Pymatgen): A Robust, Open-Source Python Library for Materials Analysis. *Comput. Mater. Sci.* **2013,** 68, 314-319.

(12) Zhu, Z.; Chu, I.-H.; Deng, Z.; Ong, S. P., Role of Na^+ Interstitials and Dopants in Enhancing the Na+ Conductivity of the Cubic Na_3PS_4 Superionic Conductor. *Chem. Mater.* **2015,** 27, (24), 8318-8325.

(13) Deng, Z.; Zhu, Z.; Chu, I.-H.; Ong, S. P., Data-Driven First-Principles Methods for the Study and Design of Alkali Superionic Conductors. *Chem. Mater.* **2016,** 29, 281-288.

(14) Wang, Y.; Richards, W. D.; Bo, S.-H.; Miara, L. J.; Ceder, G., Computational Prediction and Evaluation of Solid-State Sodium Superionic Conductors $Na_7P_3X_{11}$ (X= O, S, Se). *Chem. Mater.* **2017,** 29, 7475–7482.

(15) Lu, Z.; Ciucci, F., Structural Origin of the Superionic Na Conduction in $Na_2B_{10}H_{10}$ Closo-Borates and Enhanced Conductivity by Na Deficiency for High Performance Solid Electrolytes. *J. Mater. Chem. A* **2016,** 4, 17740-17748.

(16) Ohba, N.; Miwa, K.; Aoki, M.; Noritake, T.; Towata, S.-i.; Nakamori, Y.; Orimo, S.-i.; Züttel, A., First-Principles Study on the Stability of Intermediate Compounds of $LiBH_4$. *Phys. Rev. B* **2006,** 74, 075110.

(17) Wu, H.; Tang, W. S.; Stavila, V.; Zhou, W.; Rush, J. J.; Udovic, T. J., Structural Behavior of $Li_2B_{10}H_{10}$. *J. Phys. Chem. C* **2015,** 119, 6481-6487.

(18) Her, J.-H.; Yousufuddin, M.; Zhou, W.; Jalisatgi, S. S.; Kulleck, J. G.; Zan, J. A.; Hwang, S.-J.; Bowman Jr, R. C.; Udovic, T. J., Crystal Structure of Li2b12h12: A Possible Intermediate Species in the Decomposition of $LiBH_4$. *Inorg. Chem.* **2008,** 47, 9757-9759.

(19) Ozolins, V.; Majzoub, E.; Wolverton, C., First-Principles Prediction of Thermodynamically Reversible Hydrogen Storage Reactions in the Li-Mg-Ca-BH System. *J. Am. Chem. Soc.* **2008,** 131, 230-237.